Computers and Mathematics with Applications 167 (2024) 207–216

Contents lists available at ScienceDirect

Computers and Mathematics with Applications

journal homepage: www.elsevier.com/locate/camwa

An operator splitting method for the Cahn–Hilliard equation on nonuniform grids

Gyeonggyu Lee [a,b], Soobin Kwak [a], Yongho Choi [c], Seunggyu Lee [d,e], Seungyoon Kang [a], Seokjun Ham [a], Junseok Kim [a,*]

[a] Department of Mathematics, Korea University, Seoul 02841, Republic of Korea
[b] National Institute for Mathematical Sciences, Daejeon 34047, Republic of Korea
[c] College of Information and Communication Engineering, Computer and Information Engineering, Daegu University, Gyeongsan-si, Gyeongsangbuk-do 38453, Republic of Korea
[d] Division of Applied Mathematical Sciences, Korea University, Sejong 30019, Republic of Korea
[e] Biomedical Mathematics Group, Pioneer Research Center of Mathematical and Computational Sciences, Institute of Basic Science, Daejeon 34126, Republic of Korea

ARTICLE INFO

Keywords:
Cahn–Hilliard equation
Phase separation
Nonuniform grids

ABSTRACT

In this study, we present an operator splitting method (OSM) for the Cahn–Hilliard (CH) equation on a nonuniform mesh. The CH equation is a fourth-order partial differential equation that models phase separation phenomena in binary mixtures. Because the CH equation is applied in various scientific fields, numerous numerical methods have been developed to enhance the computational efficiency and accuracy. In this work, we consider a nonuniform mesh to improve spatial efficiency. To solve the CH equation in two-dimensional (2D) space on a nonuniform mesh, we consider the linear stabilized splitting (LSS) scheme along with the OSM. The LSS scheme is an unconditionally energy gradient stable method. To construct a simple numerical scheme, we consider the OSM in two-dimensional space. We validate that the proposed scheme satisfies the mass-preserving property. Furthermore, we conduct numerical experiments to demonstrate the efficiency and various properties of the proposed scheme.

Contents

* Corresponding author.
E-mail address: cfdkim@korea.ac.kr (J. Kim).
URL: https://mathematicians.korea.ac.kr/cfdkim/ (J. Kim).

https://doi.org/10.1016/j.camwa.2024.05.021
Received 19 September 2023; Received in revised form 15 April 2024; Accepted 16 May 2024
Available online 24 May 2024

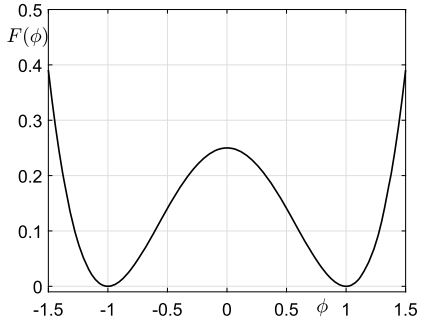

Fig. 1. Helmholtz free energy $F(\phi) = 0.25(\phi^2 - 1)^2$.

1. Introduction

We consider the Cahn–Hilliard (CH) equation on a nonuniform mesh:

$$\frac{\partial \phi(\mathbf{x},t)}{\partial t} = \Delta[F'(\phi(\mathbf{x},t)) - \epsilon^2 \Delta\phi(\mathbf{x},t)], \quad \mathbf{x} \in \Omega, \ t > 0, \tag{1}$$

where $\Omega \subset \mathbb{R}^2$. ϕ is the scalar field, ϵ is a positive constant related to interfacial thickness, and $F(\phi) = 0.25(\phi^2 - 1)^2$ is the Helmholtz free energy characterized by a double well potential [1–3,44] as shown in Fig. 1.

The CH equation is derived from the Ginzburg–Landau free energy

$$\mathcal{E}(\phi) = \int_\Omega \left(F(\phi) + \frac{\epsilon^2}{2} |\nabla \phi|^2 \right) d\mathbf{x}.$$

The zero Neumann boundary conditions are considered as

$$\mathbf{n} \cdot \nabla \phi = \mathbf{n} \cdot \nabla \Delta \phi = 0, \quad \mathbf{x} \in \partial\Omega, \ t > 0, \tag{2}$$

where $\mathbf{n}$ is the outer unit normal vector on $\partial\Omega$. By Eq. (2), we have

$$\frac{d}{dt}\mathcal{E}(\phi) = -\int_\Omega |\nabla[F'(\phi(\mathbf{x},t)) - \epsilon^2 \Delta\phi(\mathbf{x},t)]|^2 d\mathbf{x} \le 0,$$

$$\frac{d}{dt}\int_\Omega \phi d\mathbf{x} = 0.$$

Therefore, we obtain that the total free energy is non-increasing, and the total mass is conserved. The CH equation was originally developed to model the phase separation phenomenon [1]. Specifically, it describes the spinodal decomposition in binary alloys. The CH equation is a phase field model that can be applied to explain the physical phenomena in various topics such as block copolymer [4,5], vector-valued dynamics [6,7], multi-phase fluid flows [8–14], phase separation on curved surfaces [15,16], image inpainting [17–21], volume reconstruction [22–24], logarithmic free energy [25], kinetics of phase separation in iron [26], multicomponent CH systems [27], mixed systems of conductive, insulative material [28], copolymer-homopolymer mixture [29], and in arbitrary domains [30], among others. Furthermore, various numerical schemes for solving the CH equation have been developed such as the convex splitting scheme [31–34], lattice Boltzmann method [35], Saul'yev scheme [36], and Galerkin scheme [37].

The CH equation includes nonlinear and biharmonic terms, making it difficult to solve numerically. Therefore, in recent years, the convex splitting scheme is an approach for numerically solving the CH equation, which was developed by Eyre [31]. Using this scheme, we can overcome the limitations in time step size and the difficulty associated with solving the equation implicitly. The nonlinear term is numerically solved by adding some appropriate stabilization terms. Chen and Yang [32] proposed a stabilized-SAV approach for solving the anisotropic CH equation. Three linear stabilization terms remove the oscillations caused by anisotropy, while keeping the required second-order accuracy. By incorporating these linear stabilization terms, the problem reduces to solving three decoupled linear equations at each time step. Wang and Yu [33] proposed and analyzed an energy stable method for the CH gradient flow based on the stabilized linear Crank–Nicolson scheme. The authors treated the nonlinear bulk form by combining additional linear stabilization terms and showed error analysis of their proposed scheme. The nonlinear term is decomposed into the convex and the concave terms within the convex splitting scheme [34]. The authors then presented that the governing equation can be numerically solved with the convex part implicit and the concave term explicit.

The contents of this paper are as follows. In Section 3, we present our numerical scheme. In Section 4, numerical simulations are performed to validate our proposed scheme. The conclusion is given in Section 5.

2. Review of a linear stabilized splitting scheme

In this section, we discuss the linear stabilized splitting (LSS) scheme for the CH equation. The LSS scheme, a type of convex splitting method, was originally developed by Eyre [31]. It splits the convex and expansive parts of the time discretized energy functional. Then, we can construct the unconditional energy gradient stable scheme using the convexity. A numerical method is defined to be unconditionally gradient stable if the discrete total free energy is decreasing for any time step Δt. Here, we present several properties of the LSS method for the CH equation. Let ϕ^n be numerical approximation at $n\Delta t$, where Δt is the time step. The LSS scheme is written as follows [3,31]:

$$\frac{\phi^{n+1} - \phi^n}{\Delta t} = \Delta \mu^{n+\frac{1}{2}}, \ n \ge 0,$$

where $\mu^{n+\frac{1}{2}} = (\phi^n)^3 - 3\phi^n + 2\phi^{n+1} - \epsilon^2 \Delta \phi^{n+1}$. Here, the zero Neumann boundary condition is assumed. To discuss the relation between the discrete energy functional and the numerical scheme, we consider the following time discrete energy functional:

$$\mathcal{E}^n = \int_\Omega \left[F^n + \frac{\epsilon^2}{2} |\nabla \phi^n|^2 \right] d\mathbf{x},$$

where $F^n = F(\phi^n)$. When using splitting schemes to numerically solve the CH and Allen–Cahn equations, the energy stability is important [38]. Lee and Shin [39] showed mass conservation and energy stability of the compact scheme for the CH equation. Jeong et al. [40] proved the solvability and energy dissipation of various numerical scheme for the Allen–Cahn equation. Inspired by these approaches [38–40], we divide the energy functional into its convex part $\mathcal{E}_c^n$ and its expansive part $\mathcal{E}_e^n$ as follows:

$$\mathcal{E}_c^n = \int_\Omega \left[(\phi^n)^2 + \frac{\epsilon^2}{2} |\nabla \phi^n|^2 \right] d\mathbf{x}, \quad \mathcal{E}_e^n = \int_\Omega \left[-F^n + (\phi^n)^2 \right] d\mathbf{x}.$$

Then, $\mathcal{E}_c^n$ and $\mathcal{E}_e^n$ are the convex and concave functionals, respectively. Therefore, the semi discretized energy functional can be written as $\mathcal{E}^n = \mathcal{E}_c^n - \mathcal{E}_e^n$. Using the variational derivative of $\mathcal{E}^n$, we can obtain the numerical scheme as follows:

$$\frac{\phi^{n+1} - \phi^n}{\Delta t} = \Delta \left(\frac{\delta \mathcal{E}_c^{n+1}}{\delta \phi} - \frac{\delta \mathcal{E}_e^n}{\delta \phi} \right).$$

It can be interpreted as the numerical scheme as a gradient flow of the time discrete Ginzburg–Landau energy in an H^{-1}-manner. The LSS is satisfying mass preserving property:

$$\begin{aligned} \int_\Omega \phi^{n+1} d\mathbf{x} &= \int_\Omega \phi^n d\mathbf{x} + \Delta t \int_\Omega \Delta \mu^{n+\frac{1}{2}} d\mathbf{x} \\ &= \int_\Omega \phi^n d\mathbf{x} + \Delta t \int_{\partial\Omega} \mathbf{n} \cdot \left(\nabla \mu^{n+\frac{1}{2}} \right) dS = \int_\Omega \phi^n d\mathbf{x}, \end{aligned}$$

where we use the divergence theorem and the zero Neumann boundary condition. Therefore, the LSS scheme is a mass preserving scheme for

the CH equation. To discuss the properties of the considered numerical scheme, we define the following function space $\mathcal{G}$. Let us define the following function space $\mathcal{G}$:

$$\mathcal{G}=\{\phi : \int_\Omega \phi d\mathbf{x} = \int_\Omega \phi^n d\mathbf{x} \text{ for } n>0 \text{ and}$$

ϕ, μ have the homogeneous Neumann boundary condition$\}$.

To demonstrate the solvability, we proceed as follows:

(i) $(u,v)_2 = \int_\Omega uv d\mathbf{x}$.
(ii) $(u,v)_{-1} = -\int_\Omega u\Delta v d\mathbf{x}$.

Using the above definition, we can show that the LSS scheme is uniquely solvable. Given ϕ^n and $\phi \in \mathcal{G}$, we consider the following functional,

$$G(\phi) = \frac{1}{2}\|\phi\|_{-1}^2 + \Delta t\mathcal{E}_c(\phi) - (\phi^n,\phi)_{-1} + \delta t(g^n,\phi)_2$$

where $g^n = (\phi^n)^3 - 3\phi^n$. For every $\psi \in C_c^\infty(\Omega)$, the variational derivative of $G(\phi)$ is written by

$$\frac{\delta G}{\delta \phi} = (\phi - \phi^n,\psi)_{-1} + \Delta t\frac{\delta \mathcal{E}_c}{\delta \phi}(\phi) + \Delta t(g^n,\psi)_2.$$

Because $\mathcal{E}_c(\phi) = \|\phi\|_2 + \frac{\epsilon^2}{2}\|\nabla\phi\|_2^2$, we can say that

$$\frac{\delta \mathcal{E}_c}{\delta \phi}(\phi) = \left(2\phi - \epsilon^2\Delta\phi, \psi\right)_2.$$

Then, the variational derivative of G can be

$$\frac{\delta G}{\delta \phi} = (\phi - \phi^n,\psi)_{-1} + \Delta t\left(2\phi - \epsilon^2\Delta\phi + g^n,\psi\right)_2.$$

In addition, $G(\phi)$ can be convex functional because $\mathcal{E}_c(\phi)$ and $\frac{1}{2}\|\phi\|_{-1}^2$ are convex. Then, there exists a unique minimizer ϕ^{n+1} of $G(\phi)$ which is the solution of $\delta G/\delta\phi = 0$. In other words,

$$\begin{aligned}\frac{\delta G}{\delta \phi}(\phi^{n+1}) &= \left(\phi^{n+1} - \phi^n,\psi\right)_{-1} + \Delta t\left(2\phi^{n+1} - \epsilon^2\Delta\phi^{n+1} + g^n,\psi\right)_2 \\ &= \left(\phi^{n+1} - \phi^n,\psi\right)_{-1} + \Delta t\left(\mu^{n+\frac{1}{2}},\psi\right)_2 = 0.\end{aligned}$$

Therefore, we show that the LSS scheme is solvable. Next, we present that the minimizer is unique. Let us assume that $\hat{\phi}$ is another minimizer. Then, $G(\hat{\phi}) = G(\phi^*)$ and $\psi = \hat{\phi} - \phi^* \neq 0$. Using the convexity of H, we can obtain that

$$\begin{aligned}G\left(\phi^* + 0.5\psi\right) = H(0.5) &< \frac{H(0)+H(1)}{2} = \frac{G(\hat{\phi}) + G(\phi^*)}{2} = \frac{2G(\phi^*)}{2} \\ &= G(\phi^*).\end{aligned}$$

Then, $\phi^* + 0.5\psi$ is the minimizer, it contradicts that ϕ^* is the minimizer of G. In addition, we can conclude that the LSS scheme is unconditional energy stable because $\mathcal{E}_c^n$ and $\mathcal{E}_e^n$ are chosen as the convex and concave functions [45], respectively:

$$\begin{aligned}\mathcal{E}^{n+1} - \mathcal{E}^n &= \left[\mathcal{E}_c^{n+1} - \mathcal{E}_c^n\right] - \left[\mathcal{E}_e^{n+1} - \mathcal{E}_e^n\right] \le \left(\frac{\delta \mathcal{E}_c^{n+1}}{\delta\phi} - \frac{\delta \mathcal{E}_e^n}{\delta\phi}, \phi^{n+1} - \phi^n\right)_2 \\ &= \left(\mu^{n+\frac{1}{2}}, \Delta t\Delta\mu^{n+\frac{1}{2}}\right)_2 = -\Delta t\left\|\mu^{n+\frac{1}{2}}\right\|_{-1}^2 \le 0.\end{aligned}$$

3. Numerical solution algorithm

3.1. Discretization

Now, we present the discrete CH equation on a nonuniform mesh in two-dimensional (2D) space, i.e., $\Omega = (L_x, R_x)\times(L_y, R_y)$. To discuss the numerical scheme, we consider the Laplace operator Δ and biharmonic operator Δ^2 in 2D,

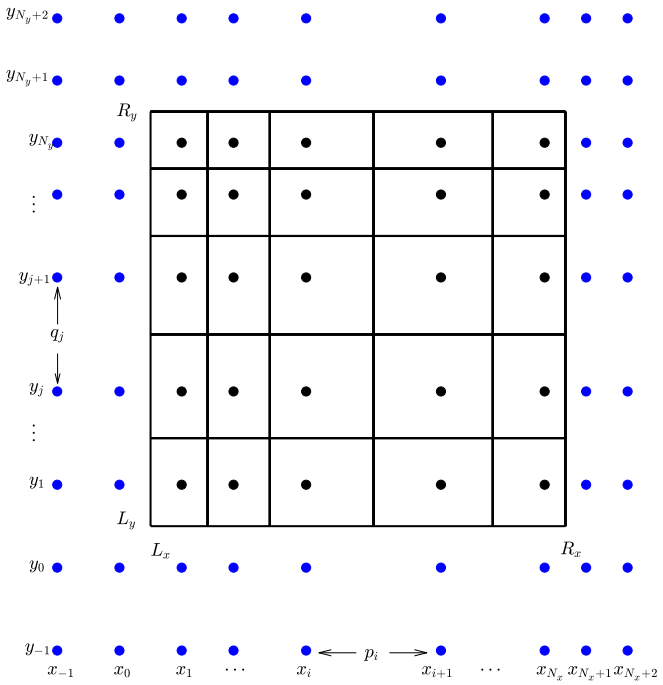

Fig. 2. Discretized domain with nonuniform mesh in 2D.

$$\Delta\phi = \frac{\partial^2\phi}{\partial x^2} + \frac{\partial^2\phi}{\partial y^2}, \quad \Delta^2\phi = \frac{\partial^4\phi}{\partial x^4} + 2\frac{\partial^4\phi}{\partial x^2\partial y^2} + \frac{\partial^4\phi}{\partial y^4}.$$

Then, the CH equation (1) is written by,

$$\begin{aligned}\frac{\partial\phi(\mathbf{x},t)}{\partial t} &= \frac{\partial^2 F'(\phi(\mathbf{x},t))}{\partial x^2} + \frac{\partial^2 F'(\phi(\mathbf{x},t))}{\partial y^2} \\ &\quad - \epsilon^2\left(\frac{\partial^4\phi(\mathbf{x},t)}{\partial x^4} + 2\frac{\partial^4\phi(\mathbf{x},t)}{\partial x^2\partial y^2} + \frac{\partial^4\phi}{\partial y^4}\right),\end{aligned} \tag{3}$$

where $\mathbf{x} = (x,y)$. To discretize the numerical scheme, we consider x_i and y_j that are nonuniform grid points in the x- and y-directions, respectively. Here, $x_i = x_{i-1} + p_{i-1}$ and $y_j = y_{j-1} + q_{j-1}$ are chosen for $i = 1,\cdots,N_x$ and $j = 1,\cdots,N_y$ where N_x and N_y are positive integers. By using the zero Neumann boundary condition, we have $p_0 = 2(x_1 - L_x)$, $p_{N_x} = 2(R_x - x_{N_x})$, $p_{-1} = p_1$, $p_{N_x+1} = p_{N_x-1}$, $q_0 = 2(y_1 - L_y)$, $q_{N_y} = 2(R_y - y_{N_y})$, $q_{-1} = q_1$, $q_{N_y+1} = q_{N_y-1}$. Let us define $p_{i+\frac{1}{2}}$ and $q_{j+\frac{1}{2}}$ as $p_{i+\frac{1}{2}} = (p_i + p_{i+1})/2$ and $q_{j+\frac{1}{2}} = (q_j + q_{j+1})/2$. The nonuniform grid points x_i and y_j are presented in Fig. 2.

Let ϕ_{ij}^n be the numerical approximation of $\phi(x_i, y_j, t_n)$. Here, $t_n = (n-1)\Delta t$ and Δt is the time step. In addition, we consider discrete operators D_{xx}, D_{yy}, D_{xxxx}, D_{xxyy} and D_{yyyy} which are the discrete operator of $\frac{\partial^2}{\partial x^2}$, $\frac{\partial^2}{\partial y^2}$, $\frac{\partial^4}{\partial x^4}$, $\frac{\partial^4}{\partial y^4}$, and $\frac{\partial^4}{\partial x^2 y^2}$, respectively. On the nonuniform mesh, these can be described as follows:

$$D_{xx}\phi_{ij} = \frac{\phi_{i+1,j} - \phi_{ij}}{p_i p_{i-\frac{1}{2}}} - \frac{\phi_{ij} - \phi_{i-1,j}}{p_{i-1}p_{i-\frac{1}{2}}} \quad \text{and}$$

$$D_{yy}\phi_{ij} = \frac{\phi_{i,j+1} - \phi_{ij}}{q_j q_{j-\frac{1}{2}}} - \frac{\phi_{ij} - \phi_{i,j-1}}{q_{j-1}q_{j-\frac{1}{2}}}.$$

The discrete Laplacian Δ_d and the discrete Biharmonic operator Δ_d^2 can be written as $D_{xx} + D_{yy}$ and $(D_{xx} + D_{yy})^2$, respectively. We discretize Eq. (3) using the LSS and the operator splitting scheme (OSM) [42]:

$$\frac{\phi_{ij}^{n+1} - \phi_{ij}^n}{\Delta t} = \Delta_d[(\phi_{ij}^n)^3 - 3\phi_{ij}^n + 2\phi_{ij}^{n+1} - \epsilon^2\Delta_d\phi_{ij}^{n+1}], \tag{4}$$

for $i = 1,\cdots,N_x$ and $j = 1,\cdots,N_y$. For the discrete CH equation (4), we consider the following OSM,

$$\phi\left(x_i, y_j, (n+1)\,\Delta t\right) = \left(\mathcal{L}_y^{\Delta t} \circ \mathcal{L}_x^{\Delta t}\right) \phi\left(x_i, y_j, n\Delta t\right).$$

Here, the operator $\mathcal{L}_x^{\Delta t}$ is defined by

$$\mathcal{L}_x^{\Delta t} u_{ij}^n = u_{ij}^{n+1},$$

where u_{ij}^{n+1} and u_{ij}^n have a relationship of

$$\frac{u_{ij}^{n+1} - u_{ij}^n}{\Delta t} = \Delta_d \left(\left(u_{ij}^n\right)^3 - 3u_{ij}^n \right) - 2\epsilon^2 D_{xx}(D_{yy} u_{ij}^n) + 2D_{xx} u_{ij}^{n+1} - \epsilon^2 D_{xx}(D_{xx} u_{ij}^{n+1}).$$

Here, u_{ij}^n is $\phi\left(x_i, y_j, n\Delta t\right)$. The operator $\mathcal{L}_y^{\Delta t}$ is defined by,

$$\mathcal{L}_y^{\Delta t} v_{ij}^n = v_{ij}^{n+1},$$

where v_{ij}^{n+1} and v_{ij}^n have a relationship of

$$\frac{v_{ij}^{n+1} - v_{ij}^n}{\Delta t} = 2D_{yy} v_{ij}^{n+1} - \epsilon^2 D_{yy}(D_{yy}) v_{ij}^{n+1}.$$

Here, v_{ij}^{n+1} is ϕ_{ij}^{n+1} and v_{ij}^n is u_{ij}^{n+1}. The zero Neumann boundary condition (2) is implemented by $\phi_{0j} = \phi_{1j}$, $\phi_{-1j} = \phi_{2j}$, $\phi_{N_x+1,j} = \phi_{N_x j}$, $\phi_{N_x+2,j} = \phi_{N_x-1,j}$, $\phi_{i0} = \phi_{i1}$, $\phi_{i,-1} = \phi_{i2}$, $\phi_{i,N_y+1} = \phi_{iN_y}$ and $\phi_{i,N_y+2} = \phi_{i,N_y-1}$. Let $\boldsymbol{\phi}^n = (\phi_{ij}^n)$.

We define the discrete energy functional on the nonuniform mesh as follows [41,43]:

$$\mathcal{E}_d(\boldsymbol{\phi}^n) = \sum_{j=1}^{N_y}\sum_{i=1}^{N_x} F(\phi_{ij}^n) p_{i-\frac{1}{2}} q_{j-\frac{1}{2}} + \frac{\epsilon^2}{2} \sum_{i=1}^{N_x-1}\sum_{j=1}^{N_y-1} \left[\frac{q_j}{p_i}\left(\phi_{i+1,j}^n - \phi_{ij}^n\right)^2 + \frac{p_i}{q_j}\left(\phi_{i,j+1}^n - \phi_{ij}^n\right)^2 \right].$$

In addition, we define the total weighted sum of ϕ^n as

$$\mathcal{M}_d(\boldsymbol{\phi}^n) = \sum_{j=1}^{N_y}\sum_{i=1}^{N_x} \phi_{ij}^n p_{i-\frac{1}{2}} q_{j-\frac{1}{2}}. \tag{5}$$

The total weighted sum of other variables can be defined similarly.

3.2. Mass preserving property

Now, we present the mass preserving property of the proposed scheme in 2D space. The discrete CH equation in 2D space is solved using two operators $\mathcal{L}_x^{\Delta t}$ and $\mathcal{L}_y^{\Delta t}$, which splits Eq. (5). Let us define $\mu_{ij}^{n+\frac{1}{2}}$ as follows:

$$\mu_{ij}^{n+\frac{1}{2}} = (\phi_{ij}^n)^3 - 3\phi_{ij}^n + 2\phi_{ij}^{n+1} - \epsilon^2 \Delta_d \phi_{ij}^{n+1}.$$

Then, Eq. (4) can be briefly written as

$$\frac{\phi_{ij}^{n+1} - \phi_{ij}^n}{\Delta t} = \Delta_d \mu_{ij}^{n+\frac{1}{2}}.$$

Applying the total weighted sum defined in Eq. (5) to both sides yields:

$$\mathcal{M}_d\left(\phi^{n+1}\right) = \mathcal{M}_d\left(\phi^n\right) + \Delta t \mathcal{M}_d\left(\Delta_d \mu^{n+\frac{1}{2}}\right).$$

From

$$D_{xx}\mu_{ij}^{n+\frac{1}{2}} p_{i-\frac{1}{2}} q_{j-\frac{1}{2}} = \left(\frac{\mu_{i+1,j}^{n+\frac{1}{2}} - \mu_{ij}^{n+\frac{1}{2}}}{p_i} - \frac{\mu_{ij}^{n+\frac{1}{2}} - \mu_{i-1,j}^{n+\frac{1}{2}}}{p_{i-1}} \right) q_{j-\frac{1}{2}},$$

and the zero Neumann boundary conditions, we can obtain the following.

$$\begin{aligned}
\mathcal{M}_d\left(D_{xx}\mu^{n+\frac{1}{2}}\right) &= \sum_{j=1}^{N_y}\sum_{i=1}^{N_x} \left(\frac{\mu_{i+1,j}^{n+\frac{1}{2}} - \mu_{ij}^{n+\frac{1}{2}}}{p_i} - \frac{\mu_{ij}^{n+\frac{1}{2}} - \mu_{i-1,j}^{n+\frac{1}{2}}}{p_{i-1}} \right) q_{j-\frac{1}{2}} \\
&= \sum_{j=1}^{N_y} q_{j-\frac{1}{2}} \sum_{i=1}^{N_x} \left(\frac{\mu_{i+1,j}^{n+\frac{1}{2}} - \mu_{ij}^{n+\frac{1}{2}}}{p_i} - \frac{\mu_{ij}^{n+\frac{1}{2}} - \mu_{i-1,j}^{n+\frac{1}{2}}}{p_{i-1}} \right) \\
&= \sum_{j=1}^{N_y} q_{j-\frac{1}{2}} \left(\frac{\mu_{N_x+1,j}^{n+\frac{1}{2}} - \mu_{N_x j}^{n+\frac{1}{2}}}{p_{N_x}} - \frac{\mu_{1j}^{n+\frac{1}{2}} - \mu_{0j}^{n+\frac{1}{2}}}{p_0} \right) = 0.
\end{aligned}$$

By applying a similar procedure to $\mathcal{M}_d\left(D_{yy}\mu^{n+\frac{1}{2}}\right)$, we conclude that

$$\mathcal{M}_d(\Delta_d \mu^{n+\frac{1}{2}}) = \mathcal{M}_d(D_{xx}\mu^{n+\frac{1}{2}}) + \mathcal{M}_d(D_{yy}\mu^{n+\frac{1}{2}}) = 0,$$
$$\mathcal{M}_d\left(\phi^{n+1}\right) = \mathcal{M}_d\left(\phi^n\right).$$

Therefore, the mass preserving property holds for the CH equation using the LSS scheme in 2D space.

4. Numerical results

In this section, we present numerical experiments using the proposed numerical scheme on nonuniform meshes. In the following numerical experiments, we refine the mesh into a nonuniform structure, with finer mesh in interesting regions and coarser resolution in less critical regions. To investigate the effect of the nonuniform mesh on the numerical results, we consider the following rectangular initial condition

$$\phi(x, y, 0) = \begin{cases} 1, & \text{if } -0.38 < x < 0.38 \text{ and } -0.22 < y < 0.22, \\ -1, & \text{otherwise.} \end{cases}$$
$$(x, y) \in \Omega = (-1, 1) \times (-1, 1)$$

with two different nonuniform meshes. The initial condition on two nonuniform meshes is shown in the first column of Fig. 3. Fig. 3 shows the temporal evolution of the numerical solution with an adaptive fine mesh, with a sufficient and tight buffer for the interface of the initial condition. Here, we use $\Delta t = 2.4691e\text{-}4$. In Fig. 3(a), the numerical solution becomes a circular shape and follows the CH dynamics. On the other hand, in Fig. 3(b), the solution is pinned and unable to accurately capture the dynamics of the CH solution.

4.1. The total energy decreasing and total mass preserving properties in 2D

Fig. 4 presents the total energy decreasing and mass preserving properties on a nonuniform mesh at each time. To perform the numerical experiments, the computational domain $\Omega_h = (0, 1)^2$ is used. The nonuniform grids p and q have random values between $0.9h$ and $1.1h$, where $h = 1/256$. The parameter ϵ, which is related to the thickness of interface, is considered as $8h/\left(2\sqrt{2}\tanh^{-1}(0.9)\right)$, and the time step Δt is set to h^2. In addition, the total iteration number is set to 1000. The initial condition is $\phi(x_i, y_j, 0) = \text{rand}(x_i, y_j)$, where $\text{rand}(x_i, y_j)$ is a random valued function between -0.1 and 0.1. The normalized total discrete energy $\mathcal{E}_h(\phi^n)/\mathcal{E}_h(\phi^0)$ and the total discrete mass $\mathcal{M}_h(\phi^n)$ are represented by black and blue lines, respectively. In addition, the snapshots present the computational results at times $250\Delta t$, $500\Delta t$, and $1000\Delta t$ from left to right, respectively. From the computational results, the proposed numerical scheme satisfies the total discrete mass preservation and energy dissipation properties on the randomly structured mesh.

We present the total energy decreasing and the mass preserving properties in a 2D subdomain on the nonuniform mesh in Fig. 5. The computational domain $\Omega_h = (0, 1)^2$ is considered. The nonuniform meshes p_i and q_j are defined as follows:

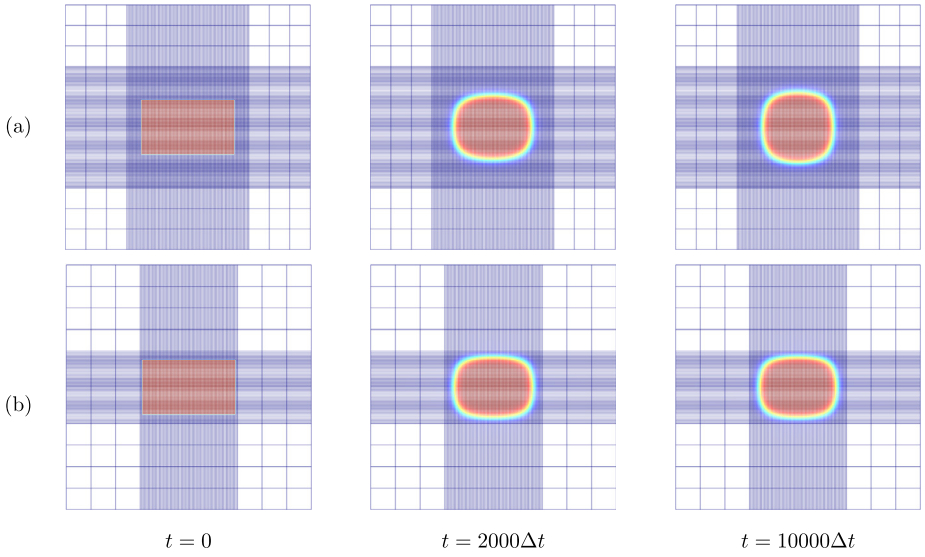

Fig. 3. Temporal evolutions of numerical solutions with an adaptive fine mesh with (a) a sufficient buffer and (b) a tight buffer for the interface of the initial condition. Here, $\Delta t = 2.4691e\text{-}4$.

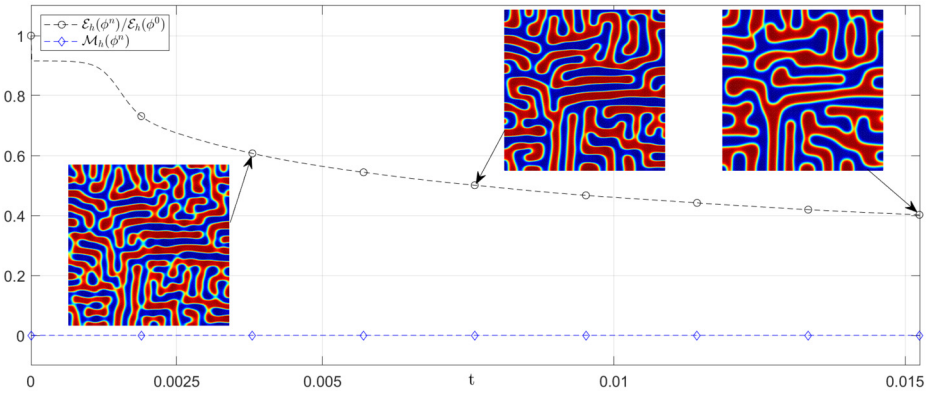

Fig. 4. Discrete total energy, discrete total mass, and snapshots at times $t = 250\Delta t, 500\Delta t$, and $1000\Delta t$ on the nonuniform mesh.

$$p_i = \begin{cases} h, & \text{if } 0.3 < x_i < 0.7, \\ 13.5h, & \text{otherwise,} \end{cases} \qquad q_j = \begin{cases} h, & \text{if } 0.3 < y_j < 0.7, \\ 13.5h, & \text{otherwise,} \end{cases}$$

where $h = 1/180$. Therefore, in Fig. 5, we consider the subdomain $(0.3, 0.7)^2$ with a fine mesh in Ω_h and a coarse mesh otherwise. $\epsilon = 2.5h/\left(2\sqrt{2}\tanh^{-1}(0.9)\right)$ and the time step $\Delta t = 0.5h^2$ are used. In addition, the final time is fixed at 0.01 and the total iteration time is set to $0.01/\Delta t$. The initial condition is

$$\phi(x_i, y_j, 0) = \begin{cases} 0.5\text{rand}(x_i, y_j) & \text{if } 0.31 < x_i, y_j < 0.69, \\ -1, & \text{otherwise,} \end{cases}$$

where $\text{rand}(x_i, y_j)$ is a random valued function between -1 and 1. In addition, Fig. 5 illustrates the snapshots at times $250\Delta t$, $500\Delta t$, and $1000\Delta t$. Fig. 5 presents the total energy and the total mass at each time. The normalized total discrete energy $\mathcal{E}_h(\phi^n)/\mathcal{E}_h(\phi^0)$ and the total discrete mass $\mathcal{M}_h(\phi^n)$ are shown as the black and blue lines, respectively. The normalized total discrete energy presents the ratio between the total discrete energy of initial condition and the energy at each time $n\Delta t$. From the results, the proposed numerical method satisfies the total discrete mass preservation and energy dissipation properties on the nonuniform mesh.

We consider a case where we have two subdomains of interest within the 2D computational domain $\Omega_h = (0, 1)^2$. The subdomains are defined as $(x_i, y_j) \in (0.15, 0.25)^2$ and $(x_i, y_j) \in (0.55, 0.85)^2$. To apply a fine mesh within these subdomains, the grid size is defined as,

$$p_i = \begin{cases} 0.2h, & \text{if } 0.1 < x_i < 0.3 \text{ and } 0.5 < x_i < 0.9, \\ h, & \text{otherwise,} \end{cases}$$

$$q_j = \begin{cases} 0.2h, & \text{if } 0.1 < y_j < 0.3 \text{ and } 0.5 < y_j < 0.9, \\ h, & \text{otherwise,} \end{cases}$$

where $h = 0.05$. Therefore, we obtain the nonuniform mesh. In each subdomain, the initial condition $\phi(x_i, y_j, 0)$ is defined as $\text{rand}(x_i, y_j)$, where $\text{rand}(x_i, y_j)$ is a random valued function between -1 and 1; elsewhere, $\phi(x_i, y_j, 0) = -1$. Note that the area of the fine mesh is larger than the domain of interest to avoid pinning effect appears when a coarse mesh with constant value is adjacent to a fine mesh with random values. Therefore, the initial condition is given by

$$\phi(x_i, y_j, 0) = \begin{cases} \text{rand}(x_i, y_j) & \text{if } 0.18 < x_i, y_j < 0.22 \\ & \text{and } 0.58 < x_i, y_j < 0.82, \\ -1, & \text{otherwise.} \end{cases}$$

The parameter values $\Delta t = 0.1h^2$ $\epsilon = 2.8h/\left(2\sqrt{2}\tanh^{-1}(0.9)\right)$ are used for this test until the final time $T = 1000\Delta t = 0.01$. Fig. 6 illustrates the snapshot images of the normalized total discrete energy $\mathcal{E}_h(\phi^n)/\mathcal{E}_h(\phi^0)$ and the total mass of phase field at $t = 250\Delta t, 500\Delta t$, and $t = 1000\Delta t$. From Fig. 6, we observe that the proposed scheme satisfies the total energy decrease and the total mass preservation.

To confirm the well-posedness of the considered numerical scheme, we evaluate the condition numbers of A_x and A_y, which are pentadi-

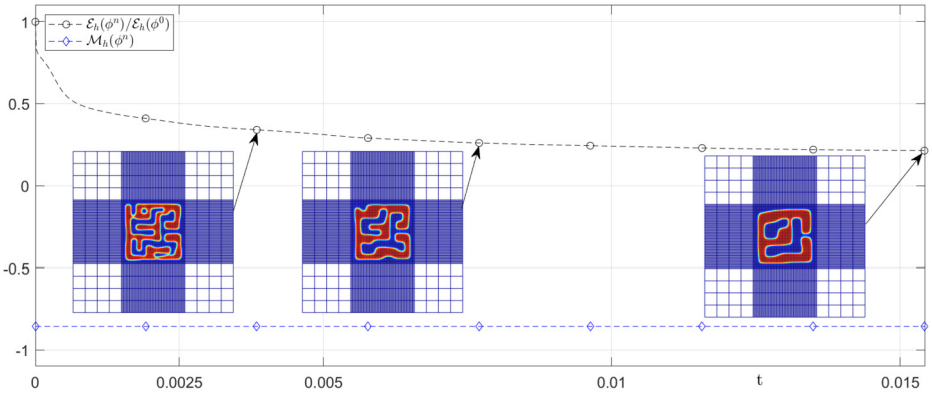

Fig. 5. Discrete total energy, discrete total mass, and snapshots at times $t = 250\Delta t, 500\Delta t$, and $1000\Delta t$ on the nonuniform mesh.

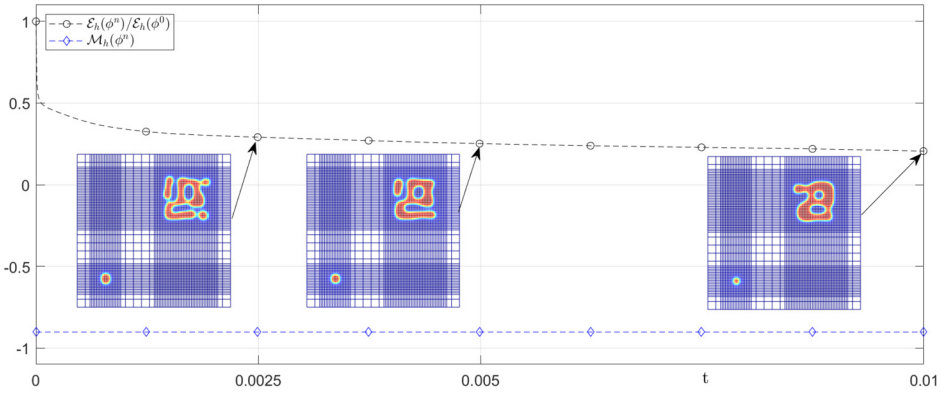

Fig. 6. Discrete total energy, discrete total mass, and snapshots at times $t = 250\Delta t, 500\Delta t$, and $1000\Delta t$ on the nonuniform mesh.

Table 1
Comparison of the condition numbers on different nonuniform grids.

k	54	27	18	13.5	10.8
Condition number of A_x	2.9998	2.9771	2.9551	2.9345	2.9151
Condition number of A_y	2.9998	2.9771	2.9551	2.9345	2.9151

agonal matrices defined by $\mathcal{L}_x$ and $\mathcal{L}_y$, respectively. There are several ways to define the condition number, such as $\|A_x\|\|A_x^{-1}\|$ or the ratio of the largest eigenvalue and the smallest eigenvalue of the matrices A_x and A_y [47,46]. In this part, we define the condition number as the ratio of the largest eigenvalue to the smallest eigenvalue of the matrices A_x and A_y [46]. To obtain the numerical result, we use the same parameters as in Fig. 5, excluding the mesh sizes p and q. The mesh sizes p and q are then applied as

$$p_i = \begin{cases} h, & \text{if } 0.3 < x_i < 0.7, \\ kh, & \text{otherwise,} \end{cases} \qquad q_j = \begin{cases} h, & \text{if } 0.3 < y_j < 0.7, \\ kh, & \text{otherwise,} \end{cases}$$

where k are chosen as 54, 27, 18, 13.5, and 10.8. We list the condition numbers of A_x and A_y for each $k = 54$, 27, 18, 13.5, and 10.8 value in Table 1. Because each condition number is strictly larger than 1 but smaller than 3, we can conclude that A is well-posed. Therefore, we can confirm that the numerical scheme is solvable.

4.2. CPU time comparison with uniform mesh and nonuniform mesh in 2D

Now, we present a comparison between the uniform and nonuniform meshes. To perform the numerical test, we use $\Omega_h = (0,1)^2$, a time step of $\Delta t = 1E-5$, and a total of 2000 iterations. In addition, the uniform grid is considered with resolutions of 1/64, 1/128, and 1/256. The nonuniform mesh is considered as

$$p_i = \begin{cases} h, & \text{if } 0.3 < x_i < 0.7, \\ 4.75h, & \text{otherwise,} \end{cases} \qquad q_j = \begin{cases} h, & \text{if } 0.3 < y_j < 0.7, \\ 4.75h, & \text{otherwise,} \end{cases}$$

where $h = 1/64$,

$$p_i = \begin{cases} h, & \text{if } 0.3 < x_i < 0.7, \\ 9.5h, & \text{otherwise,} \end{cases} \qquad q_j = \begin{cases} h, & \text{if } 0.3 < y_j < 0.7, \\ 9.5h, & \text{otherwise,} \end{cases}$$

where $h = 1/128$, and

$$p_i = \begin{cases} h, & \text{if } 0.3 < x_i < 0.7, \\ 19.25h, & \text{otherwise,} \end{cases} \qquad q_j = \begin{cases} h, & \text{if } 0.3 < y_j < 0.7, \\ 19.25h, & \text{otherwise,} \end{cases}$$

where $h = 1/256$. In each case, $\epsilon = 0.01$ and the initial condition $\phi(x_i, y_j, 0)$ is considered as

$$\phi(x_i, y_j, 0) = \begin{cases} 2\cos\left(\frac{\pi(x_i - 0.5)}{0.3}\right)\cos\left(\frac{\pi(y_j - 0.5)}{0.3}\right) - 1, & \text{if } 0.35 < x_i, y_j < 0.65, \\ -1, & \text{otherwise,} \end{cases}$$

Fig. 7 presents the evolution of ϕ_{ij}^n. Fig. 7(a) presents the evolution of ϕ_{ij}^n, the total energy, and the total mass on the nonuniform mesh. The snapshot illustrates ϕ_{ij}^n at times $1000\Delta t$, $2000\Delta t$, and $4000\Delta t$. In Fig. 7(b), we show the total mass and energy of ϕ_{ij}^n on the uniform mesh. The snapshot illustrates the $\phi(x_i, y_j, n\Delta t)$ at times $1000\Delta t$, $2000\Delta t$, and $4000\Delta t$. For Figs. 7(a) and 7(b), the discrete total energy is illustrated as the normalized total discrete energy $\mathcal{E}_h(\phi^n)/\mathcal{E}_h(\phi^0)$. Table 2 lists a comparison of CPU time with the nonuniform grid and the uniform grid at different mesh sizes. This table lists the CPU time required for the entire evolutionary process. Here, we consider the mesh sizes h with 1/64, 1/128, and 1/256. We can confirm the CPU times as 6.695982, 8.710532, and 31.912587 for uniform meshes. In addition, for the nonuniform mesh, we can confirm 1.431685, 2.731794, and 6.695982. For $h = 1/64$, the ratio of CPU time between uniform mesh and nonuniform mesh is 4.68. In addition, for $h = 1/128$ and 1/256, the

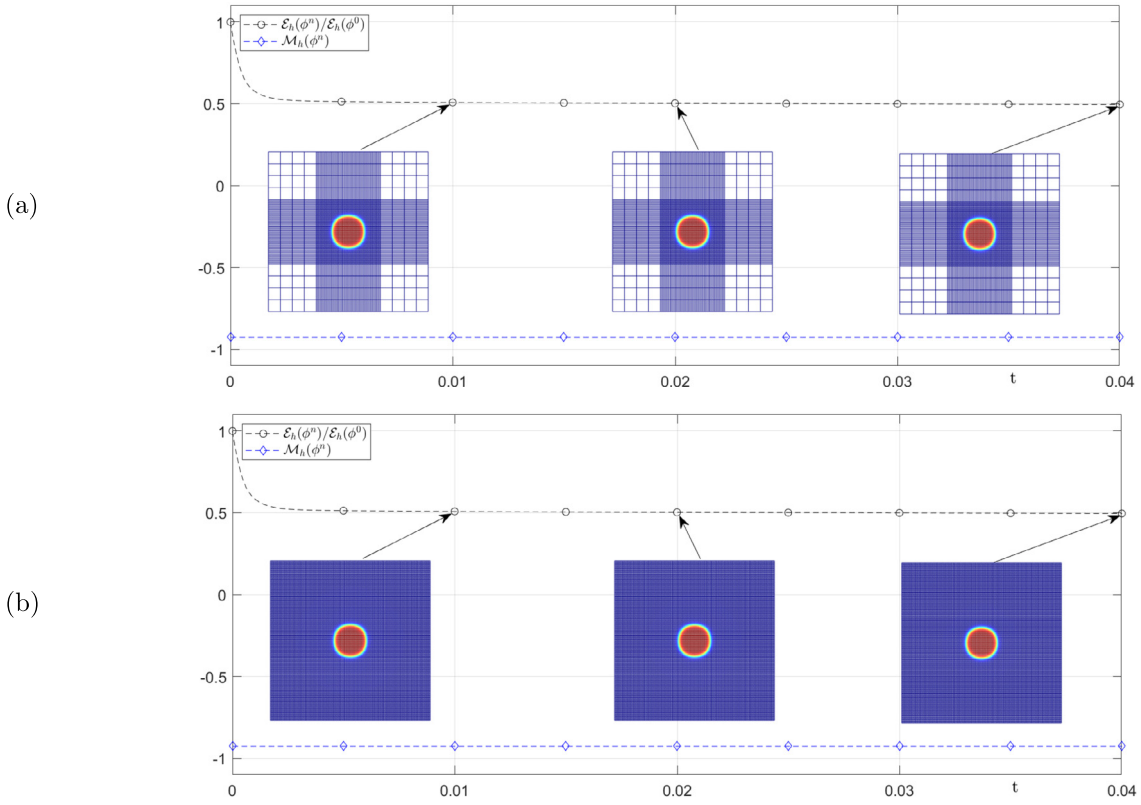

Fig. 7. Discrete total energy, discrete total mass, and snapshots at times $t = 1000\Delta t, 2000\Delta t$, and $4000\Delta t$ on the (a) nonuniform mesh and (b) uniform mesh with mesh size $h = 1/128$.

Table 2
Comparison of CPU time with uniform grid and nonuniform grid.

Grid size h	1/64	1/128	1/256
CPU time of uniform grid	6.695982	8.710532	31.912587
CPU time of nonuniform grid	1.431685	2.731794	6.695982

ratios of CPU time are 3.19 and 4.77, respectively. The numerical test is performed in MATLAB on a system with a 3.6GHz processor and 8GB RAM. In each case, we observe that the proposed numerical scheme satisfies mass preservation and energy dissipation properties. Furthermore, we can observe that the CPU time is faster on the nonuniform mesh.

4.3. Transformation from two rectangles to a circular interface

Fig. 8 presents the specific numerical result. To perform the numerical test, we consider the computational domain $\Omega_h = (-1,1)^2$. The nonuniform meshes p and q are considered as

$$p_i = \begin{cases} h, & \text{if } \ 0.3 < x_i < 0.7, \\ 13.5h, & \text{otherwise,} \end{cases} \qquad q_j = \begin{cases} h, & \text{if } \ 0.3 < y_j < 0.7, \\ 13.5h, & \text{otherwise,} \end{cases}$$

where $h = 1/90$. Here, $\Delta t = 2h^2$ and $\epsilon = 10h/(2\sqrt{2}\tanh^{-1}(0.9))$ are used. The initial condition is as follows:

$$\phi(x_i, y_j, 0) = \tanh\left(\frac{-\max\left(|x_i + 0.15| - 0.1, |y_j| - 0.23\right)}{\sqrt{2}\epsilon}\right) + \tanh\left(\frac{-\max\left(|x_i - 0.15| - 0.1, |y_j| - 0.23\right)}{\sqrt{2}\epsilon}\right) + 1.$$

In Fig. 8(a)–(d), we present the computational results at times $t = 0$, $100\Delta t$, $500\Delta t$, and $1000\Delta t$, respectively. In Fig. 8, we can observe that the two rectangular-shaped interfaces merge into one circular interface.

In addition, we consider two subdomains for numerical simulation as shown in Fig. 9. Here, the computational domain is $\Omega_h = (0,10)^2$, and the subdomains are $(1,3.5)^2$ and $(7,8.5)^2$, which are constructed using a fine mesh. The nonuniform mesh p and q are considered as

$$p_i = \begin{cases} h, & \text{if } \ 1 < x_i < 3.5 \ \text{ and } \ 7 < x_i < 8.5, \\ 6h, & \text{otherwise,} \end{cases}$$

$$q_j = \begin{cases} h, & \text{if } \ 1 < y_j < 3.5 \ \text{ and } \ 0.5 < y_j < 8.5, \\ 6h, & \text{otherwise,} \end{cases}$$

where $h = 0.05$. $\epsilon = 8h/\left(2\sqrt{2}\tanh^{-1}(0.9)\right)$ and time step $\Delta t = h^2$ are used. The initial condition is defined as $\phi(x_i, y_j, 0) = 1$ if $(x_i, y_j) \in (1.2, 2.1) \times (1.2, 3.3)$, $(2.4, 3.3) \times (1.2, 3.3)$, $(7.2, 7.6) \times (7.1, 8.4)$ and $(7.9, 8.3) \times (7.1, 8.4)$; otherwise, $\phi(x_i, y_j, 0) = -1$. Here, we can observe that the two small rectangles shrink to a circle at time $150\Delta t$. After then, the two larger rectangles shrink to one.

4.4. Transformation from two circles to a circular interface

Now, we present the evolution of two circular shape initial conditions. In Fig. 10 present the specific numerical results. To perform the numerical test, we consider the computational domain $\Omega_h = (-1,1)^2$. The nonuniform mesh p and q are considered as follows:

$$p_i = \begin{cases} h, & \text{if } \ 0.3 < x_i < 0.7, \\ 22.5h, & \text{otherwise,} \end{cases}$$

$$q_j = \begin{cases} h, & \text{if } \ 0.3 < y_j < 0.7, \\ 22.5h, & \text{otherwise,} \end{cases}$$

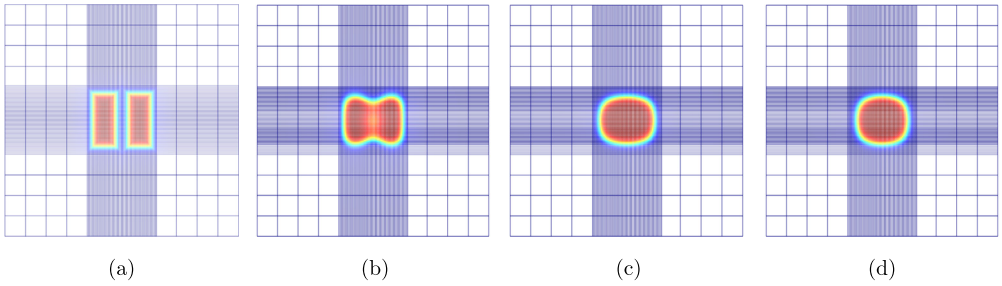

Fig. 8. Evolution of two rectangular-shaped initial conditions: (a) initial condition, (b) $t = 100\Delta t$, (c) $t = 500\Delta t$, and (d) $t = 1000\Delta t$.

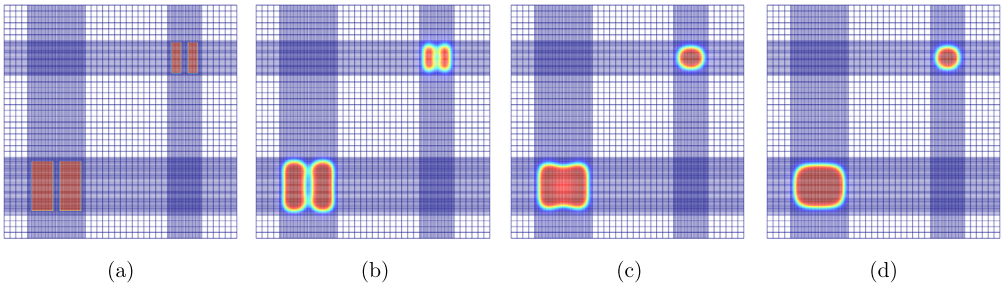

Fig. 9. Evolution of two rectangular-shaped initial conditions: (a) initial condition, (b) $t = 30\Delta t$, (c) $t = 150\Delta t$, and (d) $t = 300\Delta t$.

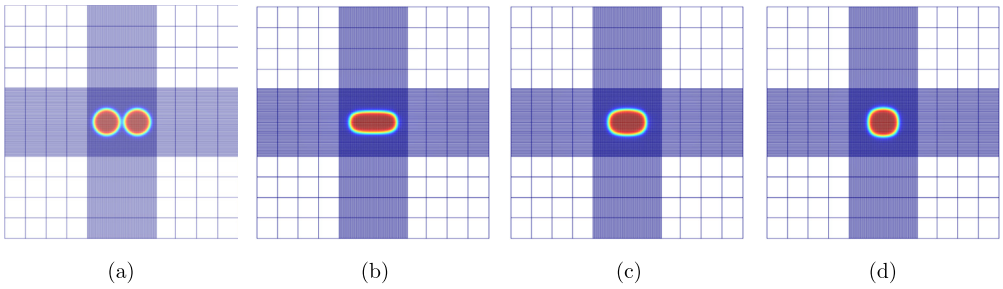

Fig. 10. Evolution of two box shaped initial condition: (a) initial condition, (b) $t = 875\Delta t$, (c) $t = 1750\Delta t$, and (d) $t = 3500\Delta t$.

where $h = 1/128$. Here, we use some computational parameters $\Delta t = h^2$, $\epsilon = 8h/(2\sqrt{2}\tanh^{-1}(0.9))$. The initial condition is considered as

$$\phi(x_i, y_j, 0) = \tanh\left(\frac{\left(0.11 - \sqrt{(x_i + 0.13)^2 + y_j^2}\right)}{\sqrt{2}\epsilon}\right) + \tanh\left(\frac{\left(0.11 - \sqrt{(x_i - 0.13)^2 + y_j^2}\right)}{\sqrt{2}\epsilon}\right) + 1.$$

In Fig. 10(a)–(d), we present the computational results at times $t = 0$, $875\Delta t$, $1750\Delta t$, and $3500\Delta t$, respectively. In Fig. 10, we can observe that the two circular shaped interfaces merge into a single circular interface.

In addition, we consider two subdomains for computational simulations as shown in Fig. 11. Here, the computational domain is $\Omega_h = (0,1)^2$, and the subdomains are $(0.1, 0.3)^2$ and $(0.5, 0.9)^2$, which are constructed using a fine mesh. The nonuniform mesh p and q are considered as

$$p_i = \begin{cases} h, & \text{if } 0.1 < x_i < 0.3 \text{ and } 0.5 < x_i < 0.9, \\ 10h, & \text{otherwise,} \end{cases}$$

$$q_j = \begin{cases} h, & \text{if } 0.1 < y_j < 0.3 \text{ and } 0.5 < y_j < 0.9, \\ 10h, & \text{otherwise,} \end{cases}$$

where $h = 0.05$. The interfacial parameter $\epsilon = 6h/\left(2\sqrt{2}\tanh^{-1}(0.9)\right)$ and time step $\Delta t = h^2$ are used. The initial condition is as follows:

$$\phi(x_i, y_j, 0) = \begin{cases} 1, & \text{if } (x_i, y_j) \in \bigcup_{k=1}^{4} C_k, \\ -1, & \text{otherwise,} \end{cases}$$

where C_k is a circle shaped subdomain. C_1 and C_2 are circles with radii of 0.13 with centers at (1.5,2) and (2.5,2), respectively. C_3 and C_4 are circles with radii of 0.7 with centers at (6.2,7) and (7.8,7), respectively. Initial condition is illustrated in Fig. 11. We can observe that the two small circles shrink to one circle by time $500\Delta t$. After then, the two large boxes also shrink to one.

To investigate more complex dynamics, we consider two subdomains for numerical simulation as shown in Fig. 12. Here, the computational domain is $\Omega_h = (0,1)^2$, and the subdomains are $(0.1, 0.3)^2$ and $(0.5, 0.9)^2$, which are constructed by a fine mesh. Otherwise, we use a coarse mesh. The nonuniform mesh p and q are considered as

$$p_i = \begin{cases} h, & \text{if } 0.1 < x_i < 0.3, \text{ and } 0.5 < x_i < 0.9, \\ 10h, & \text{otherwise,} \end{cases}$$

$$q_j = \begin{cases} h, & \text{if } 0.1 < y_j < 0.3, \text{ and } 0.5 < y_j < 0.9, \\ 10h, & \text{otherwise,} \end{cases}$$

where $h = 0.05$. $\epsilon = 6h/\left(2\sqrt{2}\tanh^{-1}(0.9)\right)$ and time step $\Delta t = h^2$ are used. The initial condition is defined as follows:

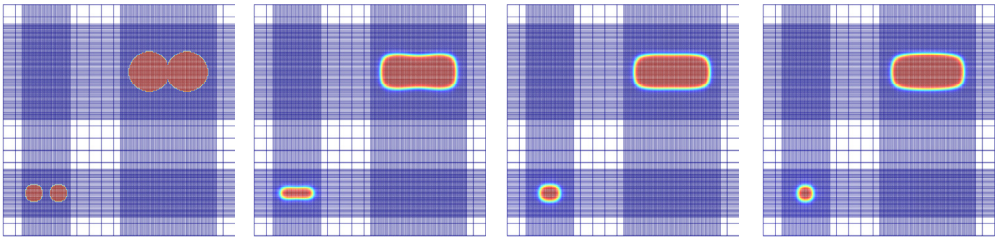

Fig. 11. Evolution of two box-shaped initial conditions: (a) initial condition, (b) $t = 250\Delta t$, (c) $t = 750\Delta t$, and (d) $t = 1000\Delta t$.

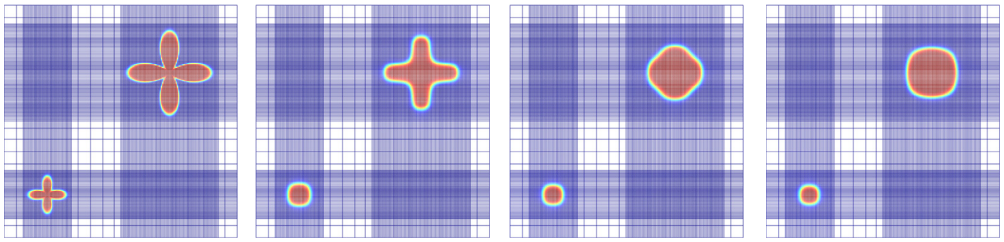

Fig. 12. Evolution of flower shaped initial condition: (a) initial condition, (b) $t = 250\Delta t$, (c) $t = 750\Delta t$, and (d) $t = 1000\Delta t$.

$$\phi(x_i, y_j, 0) = \tanh\left(\frac{0.5 + 0.25\cos(4\theta_1(x_i, y_j)) - \sqrt{(x_i-2)^2 + (y_j-2)^2)}}{\sqrt{2}\epsilon}\right) + \tanh\left(\frac{(1 + 0.7\cos(4\theta_2(x_i, y_j)) - \sqrt{(x_i-7)^2 + (y_j-7)^2}}{\sqrt{2}\epsilon}\right) + 1,$$

where $\theta_1(x, y) = \tan^{-1}((y-2)/(x-2))$ and $\theta_2(x, y) = \tan^{-1}((y-7)/(x-7))$. Initial condition is illustrated in Fig. 12(a). Figs. 12(a)–(d) present the computational results at times $t = 0\Delta t$, $250\Delta t$, $750\Delta t$, and $1000\Delta t$, respectively. We can observe that the flower-shaped interface shrinks to a rectangle, and the rectangular-shaped interface deforms into a circle.

5. Conclusions

In this paper, we presented the unconditionally energy stable numerical scheme using the LSS and OSM for the CH equation on nonuniform meshes. The CH equation is widely used for modeling for the phase separation phenomena. Therefore, the enhancement of the efficiency is important. We presented stable numerical schemes on nonuniform grids to improve the efficiency for the space. We presented the numerical analysis that the proposed scheme satisfies the mass preserving property. In addition, because we used the linear stabilized scheme and operator splitting scheme, the proposed numerical scheme is practically stable scheme. We have presented the numerical experiments to demonstrate the efficiency by comparison with the uniform mesh. The strategy for constructing a nonuniform mesh is an important subject, as it can cause global refinement and significantly affect accuracy and efficiency. In the future work, we can improve nonuniform mesh construction adaptively based on time-varying numerical solutions. We can also consider some application works such as image inpainting and volume reconstruction using this numerical scheme to enhance efficiency.

Data availability

The authors do not have permission to share data.

Acknowledgements

The first author (Gyeonggyu Lee) was supported by the National Institute for Mathematical Sciences (NIMS) granted by the Korea government (No. NIMS-B24910000). The corresponding author (J.S. Kim) was supported by the Brain Korea 21 FOUR from the Ministry of Education of Korea. The authors are grateful to the reviewers for their valuable feedback, which has enhanced the quality of this article.

References

[1] J.W. Cahn, J.E. Hilliard, Free energy of a non-uniform system. I. Interfacial free energy, J. Chem. Phys. 28 (1958) 258–267.
[2] H. Kim, C. Lee, S. Kwak, Y. Hwang, S. Kim, Y. Choi, J. Kim, Three-dimensional volume reconstruction from multi-slice data using a shape transformation, Comput. Math. Appl. 113 (2022) 52–58.
[3] S. Lee, C. Lee, H. Lee, J. Kim, Comparison of different numerical schemes for the Cahn–Hilliard equation, J. Korean Soc. Ind. Appl. Math. 17 (3) (2013) 197–207.
[4] J.B. Berg, J.F. Williams, Validation of the bifurcation diagram in the 2D Ohta–Kawasaki problem, Nonlinearity 30 (4) (2017) 1584.
[5] Q. Li, L. Mei, Efficient, decoupled, and second-order unconditionally energy stable numerical schemes for the coupled Cahn–Hilliard system in copolymer/homopolymer mixtures, Comput. Phys. Commun. 260 (2021) 107290.
[6] Z. Guo, F. Yu, S. Wise, J. Lowengrub, A diffuse domain method for two-phase flows with large density ratio in complex geometries, J. Fluid Mech. 907 (2021) A38.
[7] W. Chen, C. Wang, S. Wang, X. Wang, S.M. Wise, Energy stable numerical schemes for ternary Cahn–Hilliard system, J. Sci. Comput. 84 (2) (2020) 1–36.
[8] P.H. Chiu, A coupled phase field framework for solving incompressible two-phase flows, J. Comput. Phys. 392 (1) (2019) 115–140.
[9] H.L. Li, H.R. Liu, H. Ding, A fully 3D simulation of fluid-structure interaction with dynamic wetting and contact angle hysteresis, J. Comput. Phys. 420 (1) (2020) 109709.
[10] J.T. Zhang, H.R. Liu, H. Ding, Head-on collision of two immiscible droplets of different components, Phys. Fluids 32 (8) (2020) 082106.
[11] H. Liang, B.C. Shi, Z.H. Chai, Lattice Boltzmann modeling of three-phase incompressible flows, Phys. Rev. E 93 (1) (2016) 013308.
[12] L. Zhwng, S. Zheng, Q. Zhai, Reduction-consistent Cahn–Hilliard theory based lattice Boltzmann equation method for N immiscible incompressible fluids, Physica A 574 (2021) 126015.
[13] J. Yang, J. Kim, A phase-field method for two-phase fluid flow in arbitrary domains, Comput. Math. Appl. 79 (2020) 1857–1874.
[14] Q. Xia, J. Kim, B. Xia, Y. Li, An unconditionally energy stable method for binary incompressible heat conductive fluids based on the phase–field model, Comput. Math. Appl. 123 (2022) 26–39.
[15] F. Amiri, S. Ziaei-Rad, N. Valizadeh, T. Rabczu, On the use of local maximum entropy approximants for Cahn–Hilliard phase-field models in 2D domains and on surfaces, Comput. Methods Appl. Mech. Eng. 346 (2019) 1–24.

[16] D. Jeong, Y. Li, C. Lee, J. Yang, J. Kim, A conservative numerical method for the Cahn–Hilliard equation with generalized mobilities on curved surfaces in three-dimensional space, Commun. Comput. Phys. 27 (2020) 412–430.
[17] A.L. Brkic, D. Mitrovic, A. Novak, On the image inpainting problem from the viewpoint of a nonlocal Cahn–Hilliard type equation, J. Adv. Res. 25 (2020) 67–76.
[18] A. Bertozzi, C.B. Schönlieb, Unconditionally stable schemes for higher order inpainting, Commun. Math. Sci. 9 (2) (2011) 413–457.
[19] J. Bosch, D. Kay, M. Stoll, A.J. Wathen, Fast solvers for Cahn–Hilliard inpainting, SIAM J. Imaging Sci. 7 (1) (2014) 67–97.
[20] H. Garcke, K.F. Lam, V. Styles, Cahn–Hilliard inpainting with the double obstacle potential, SIAM J. Imaging Sci. 11 (3) (2018) 2064–2089.
[21] N. Andrej, N. Reinić, Shock filter as the classifier for image inpainting problem using the Cahn–Hilliard, Comput. Math. Appl. 123 (2022) 105–114.
[22] Y. Li, J. Wang, B. Lu, D. Jeong, J. Kim, Multicomponent volume reconstruction from slice data using a modified multicomponent Cahn–Hilliard system, Pattern Recognit. 93 (2019) 124–133.
[23] J. Kim, C. Lee, Three-dimensional volume reconstruction using two-dimensional parallel slices, SIAM J. Imaging Sci. 12 (1) (2019) 1–27.
[24] Y. Choi, S. Lee, Three-dimensional volume reconstruction based on modified fractional Cahn–Hilliard equation, J. Korean Soc. Ind. Appl. Math. 23 (3) (2019) 203–210.
[25] W. Chen, C. Wang, X. Wang, S.M. Wise, Positivity-preserving, energy stable numerical schemes for the Cahn–Hilliard equation with logarithmic potential, J. Comput. Phys. 3 (2019) 100031.
[26] D. Lu, M.S. Osman, M.M.A. Khter, R.A.M. Attia, D. Baleanu, Analytical and numerical simulations for the kinetics of phase separation in iron (Fe–Cr–X (X= Mo, Cu)) based on ternary alloys, Physica A 574 (2020) 126015.
[27] S. Zhou, Y.M. Xie, Numerical simulation of three-dimensional multicomponent Cahn–Hilliard systems, Int. J. Mech. Sci. 198 (2021) 106349.
[28] Y. Nagamine, Numerical analysis of phase separation between conductive and insulative materials induced under constant current mode using the extended Cahn–Hilliard equation, Physica A 604 (2022) 127925.
[29] J. Wu, Z. Xin, Z. Tan, An unconditionally energy stable algorithm for copolymer-homopolymer mixtures, Int. J. Mech. Sci. 238 (2023) 107846.
[30] J. Kim, Z. Tan, J. Yang, Linear and conservative IMEX Runge–Kutta finite difference schemes with provable energy stability for the Cahn–Hilliard model in arbitrary domains, Comput. Math. Appl. 143 (2023) 133–150.
[31] D.J. Eyre, An unconditionally stable one-step scheme for gradient systems, 1997, Unpublished.
[32] C. Chen, X. Yang, Fast, provably unconditionally energy stable, and second-order accurate algorithms for the anisotropic Cahn–Hilliard model, Comput. Methods Appl. Mech. Eng. 351 (2019) 35–59.
[33] L. Wang, H. Yu, An energy stable linear diffusive Crank–Nicolson scheme for the Cahn–Hilliard gradient flow, J. Comput. Appl. Math. 377 (2020) 112880.
[34] J. Guo, C. Wang, S. Wise, X. Yue, An H^2 convergence of a second-order convex-splitting, finite difference scheme for the three-dimensional Cahn–Hilliard equation, Commun. Math. Sci. 14 (2016) 489–515.
[35] H. Liang, C. Zhang, R. Du, Y. Wei, Lattice Boltzmann method for fractional Cahn–Hilliard equation, Commun. Nonlinear Sci. Numer. Simul. 91 (2020) 105443.
[36] J. Yang, Y. Li, C. Lee, H.G. Lee, S. Kwak, Y. Hwang, X. Xin, J. Kim, An explicit conservative Saul'yev scheme for the Cahn–Hilliard equation, Int. J. Mech. Sci. 217 (2022) 106985.
[37] W. Zhao, Q. Guan, Numerical analysis of energy stable weak Galerkin schemes for the Cahn–Hilliard equation, Commun. Nonlinear Sci. Numer. Simul. 118 (2023) 106999.
[38] J. Shen, X. Yang, Numerical approximations of Allen–Cahn and Cahn–Hilliard equations, Discrete Contin. Dyn. Syst. 28 (4) (2010) 1669–1691.
[39] S. Lee, J. Shin, Energy stable compact scheme for Cahn–Hilliard equation with periodic boundary condition, Comput. Math. Appl. 77 (1) (2019) 189–198.
[40] D. Jeong, S. Lee, D. Lee, J. Shin, J. Kim, Comparison study of numerical methods for solving the Allen–Cahn equation, Comput. Mater. Sci. 111 (2016) 131–136.
[41] Y. Choi, D. Jeong, J. Kim, A multigrid solution for the Cahn–Hilliard equation on nonuniform grids, Appl. Math. Comput. 293 (2017) 320–333.
[42] V. Calo, P. Minev, V. Puzyrev, Splitting schemes for phase-field models, Appl. Numer. Math. 156 (2020) 192–209.
[43] J. Kim, H. Bae, An unconditionally gradient stable adaptive mesh refinement for the Cahn–Hilliard equation, J. Korean Phys. Soc. 53 (2) (2008).
[44] S. Lee, Unconditionally strong energy stable scheme for Cahn–Hilliard equation with second-order temporal accuracy, Math. Methods Appl. Sci. 46 (6) (2023) 6463–6469.
[45] S.M. Wise, C. Wang, J.S. Lowengrub, An energy-stable and convergent finite-difference scheme for the phase field crystal equation, SIAM J. Numer. Anal. 47 (3) (2009) 2269–2288.
[46] Y.C. Hon, X.Z. Mao, An efficient numerical scheme for Burgers' equation, Appl. Math. Comput. 95 (1) (1998) 37–50.
[47] A.K. Cline, C.B. Moler, G.W. Stewart, J.H. Wilkinson, An estimate for the condition number of a matrix, SIAM J. Numer. Anal. 16 (2) (1979) 368–375.